Journal of Sol-Gel Science and Technology
https://doi.org/10.1007/s10971-025-07008-9

ORIGINAL PAPER

Structure-property tailoring of forsterite ceramic via sol-gel processing with controlled dielectric properties

Ahcene Keziz[1] · Menad Heraiz[1] · Linda Aissani[2] · Taha Abdel Mohaymen Taha[3] · Rachid Makhloufi[4]

Received: 20 August 2025 / Accepted: 13 October 2025

Abstract

Due to the rapid development of telecommunications systems toward 5G and 6G, there is a high demand for dielectric materials with low dielectric permittivity and low tangent. In this study presents a comprehensive investigation of sol–gel derived forsterite (Mg_2SiO_4) ceramics, focusing on their structural, microstructural, and dielectric properties. XRD and Rietveld-refinement analysis confirmed phase-pure orthorhombic forsterite (space group *Pbnm*) with no secondary phases. FESEM/EDS analysis revealed a well-defined microstructure and stoichiometric Mg_2SiO_4 composition (Mg:Si:O ≈ 2:1:4 atomic ratio). The bulk density was measured as 2.56 g/cm^3, corresponding to ~78% of theoretical density. Dielectric and impedance spectroscopy studies demonstrated excellent functional properties: low relative permittivity ($\varepsilon_r \sim 9.12$ at 1 MHz) and minimal loss tangent ($\tan\delta < 0.015$). Complex impedance analysis showed a decrease in the real part of impedance (Z') with increasing frequency and temperature, while Nyquist plots exhibited single semicircular arcs, indicative of non-Debye relaxation dominated by grains. Electrical modulus spectra revealed relaxation peaks shifting to higher frequencies with temperature. The exponent *s* decreased from 1.85 (100 °C) to 1.76 (400 °C), indicating correlated barrier hopping (CBH) conduction. The DC conductivity followed Arrhenius behavior with an activation energy (E_a) of 0.19 eV, consistent with polaron-assisted transport. This work established structure-property relationships linking sol–gel processing, microstructure, and optimized dielectric performance.

Graphical Abstract

This work successfully demonstrated the synthesis of high-performance forsterite (Mg_2SiO_4) ceramics via a controlled sol–gel process. Dielectric spectroscopy studies demonstrated excellent functional properties: low relative permittivity (ε_r ~9.12 at 1 MHz) and minimal loss tangent ($\tan\delta < 0.015$).

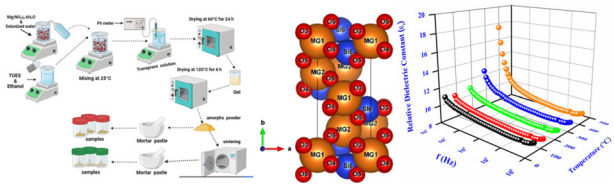

Keywords Forsterite · Sol gel · Rietveld-refinement · Dielectric spectroscopy · Activation energy

✉ Ahcene Keziz
ahcen.keziz@univ-msila.dz

✉ Taha Abdel Mohaymen Taha
taha.hemida@yahoo.com

[1] Department of Physics, Physics and Chemistry of Materials Laboratory, University Pole, M'sila, Algeria

[2] Matter Sciences Department, Institute of ST Abbes Laghrour University Khenchela, Khenchela, Algeria

[3] Physics and Engineering Mathematics Department, Faculty of Electronic Engineering, Menoufia University, Menouf 32952, Egypt

[4] Laboratory of Applied Chemistry (LCA), University of Biskra, Biskra, Algeria

Published online: 29 October 2025

Highlights

- Sol–gel synthesis yielded stoichiometric forsterite (Mg:Si:O ≈ 2:1:4).
- Rietveld-refinement analysis confirmed phase-pure orthorhombic forsterite.
- Excellent dielectric properties of forsterite with low permittivity (ε_r ~9.12) and loss.
- Correlated barrier hopping (CBH) is the dominant conduction mechanism.
- Low activation energy (0.19 eV) of forsterite suggested polaron-assisted transport.

1 Introduction

The accelerating pace of technological innovation, particularly in 5G wireless communication systems, has created exceptional demand for high-performance dielectric ceramic materials [1, 2]. These ceramics serve as essential substrates in 5G components due to their unique ability to meet three critical requirements simultaneously: optimal dielectric constants for signal integrity, ultra-low loss tangents for energy efficiency, and excellent thermal stability for reliability under high-frequency operation [2, 3]. Besides telecommunications, their exceptional electrical insulation, thermal management capabilities, and frequency stability make them indispensable across diverse applications - from aerospace radar systems and satellite communications to medical imaging devices and next-generation electronic packaging [3, 4]. The ongoing miniaturization of 5G infrastructure and Internet of Things (IoT) devices further intensifies the need for ceramics with precisely tunable dielectric properties, driving extensive research into material composition and microstructure engineering. These technological imperative positions dielectric ceramics as enablers of future breakthroughs across multiple industries that depend on high-frequency, high-reliability electronic systems.

Dielectric ceramic materials hold significant technological importance due to their diverse applications across multiple industries [4–7]. For optimal performance in high-frequency applications, these ceramics should possess a low dielectric permittivity (ε_r) to minimize signal propagation delay (T_{pd}), since $T_{pd} \propto \sqrt{\varepsilon_r}$. Additionally, signal attenuation (α_s) follows the relationship $a_s = \frac{Af\sqrt{\varepsilon_r}}{Q}$, where f is frequency and Q is the quality factor [3–5]. As wireless communication frequencies increase, maintaining signal integrity requires ceramics with exceptionally high Q factors ($Q = 1/\tan(\delta)$) to reduce energy losses.

Among the industrially relevant materials in the MgO-SiO_2 system, forsterite (Mg_2SiO_4) - comprising 57.29 wt% MgO and 42.71 wt% SiO_2 [3–7] - has emerged as a particularly valuable phase. This ceramic exhibited outstanding dielectric properties ($\varepsilon_r \sim 6$–7, $Q \sim 240{,}000$ GHz), coupled with low thermal expansion, high hardness (7.68 GPa), exceptional thermal stability (melting point 1890 °C), and excellent chemical resistance [8–11]. These characteristics make it ideal for diverse applications: in biomedicine, it promotes bone regeneration through enhanced bioactivity [11–13]; in electronics, it serves as an insulating substrate for microwave and laser technologies [14–16]; and in refractory applications, it withstands extreme thermal conditions. Various synthesis methods, including polymer precursor [17], hydrothermal [18], solid-state [19], and mechanical activation [10] techniques, have been developed to produce high-purity forsterite at reduced calcination temperatures, further enhancing its commercial viability.

Several benefits make the sol–gel method more feasible than other synthesis techniques such as co-precipitation, hydrothermal, or solid-state reactions [7–14]. It enables synthesis at relatively low processing temperatures compared to conventional solid-state reactions that require very high calcination, thereby preserving fine structural features. The method also ensures high purity and superior chemical homogeneity through molecular-level precursor mixing, which is often difficult to achieve with solid-state techniques. In addition, the sol–gel route offers controlled microstructural features, allowing adjustment of particle size, porosity, and surface area factors that are crucial for tailoring the electrical, optical, or biomedical properties of ceramics. Consequently, materials synthesized via sol–gel often exhibit improved functional properties, particularly enhanced dielectric, optical, or bioactive performance compared to those prepared by traditional methods.

Compared to earlier works, the novelty of the present study lies in its efficient sol–gel synthesis at lower processing costs, phase-pure high-crystallinity forsterite, detailed microstructural insights, comprehensive dielectric analysis across broad frequencies. Forsterite (Mg_2SiO_4) precursor powder was prepared via the sol–gel method using tetraethyl orthosilicate (TEOS) and magnesium nitrate hexahydrate ($Mg(NO_3)_2{\cdot}6H_2O$) as starting materials, with detailed characterization of samples sintered at 1450 °C for 1 h. X-ray diffraction (XRD) analysis confirmed the formation of phase-pure orthorhombic forsterite (space group *Pbnm*) with high crystallinity. Field-emission scanning electron microscopy (FESEM) revealed a well-defined microstructure characterized by distinct grains separated by grain boundaries. Grain boundaries were clearly resolved, with energy-dispersive spectroscopy (EDS) verifying stoichiometric Mg_2SiO_4 composition. This work further investigated the dielectric and AC conductivity properties of sintered pellets across a wide frequency range (0.1 kHz–1 MHz). Frequency-dependent

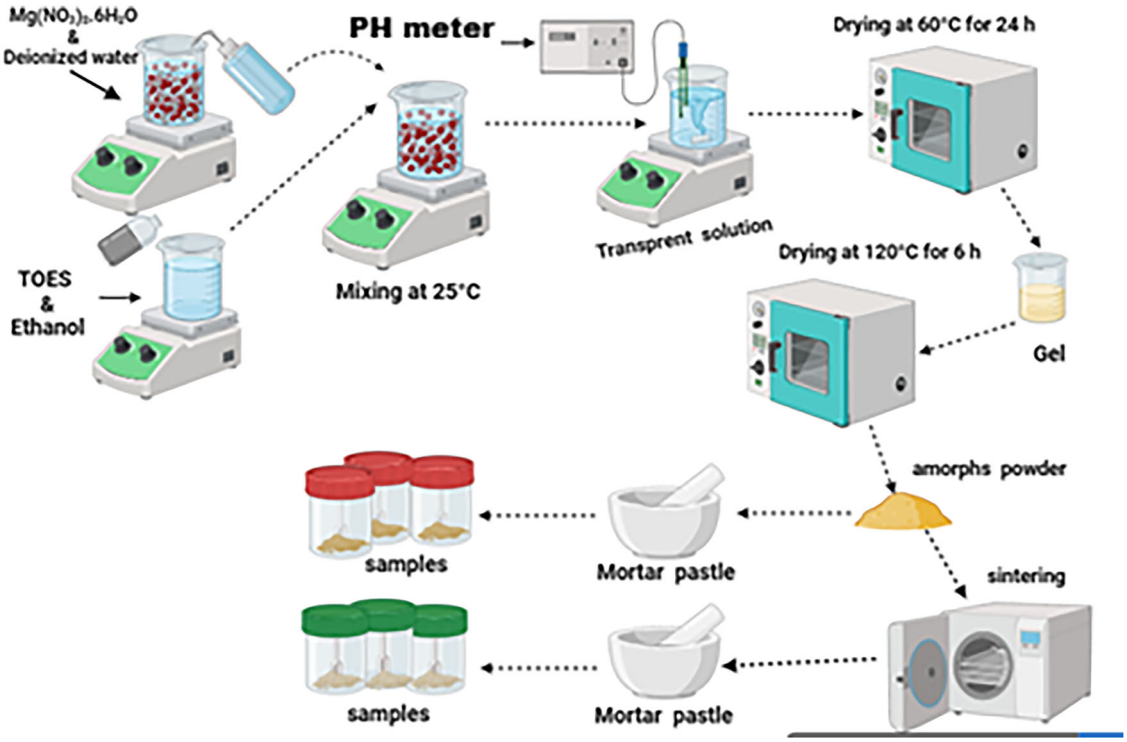

Fig. 1 Flow chart of the synthesis of forsterite powder

permittivity and loss tangent trends correlated with microstructural features observed in SEM, where grain boundary effects dominated low-frequency responses while bulk contributions prevailed at higher frequencies. AC conductivity analysis, supported by Jonscher's power law, identified hopping conduction as the dominant mechanism, with activation energies derived from Arrhenius plots.

2 Materials and methods

2.1 Materials

Magnesium nitrate hexahydrate ($Mg(NO_3)_2{\cdot}6H_2O$) was procured from Biochem Chemopharma (Georgia, USA), serving as the magnesium source for the synthesis. Tetraethyl orthosilicate (TEOS, $Si(C_2H_5O)_4$, 99% purity) was obtained from Fluka and acted as the silicon precursor, while absolute ethanol (CH_3CH_2OH, ≥99.8% purity) from Sigma-Aldrich was used as the solvent. These high-purity reagents were deliberately selected to minimize impurities that could affect the synthesis process or the final properties of the forsterite material.

2.2 Processing of powders

The forsterite precursor was prepared via a sol–gel method (see Fig. 1) using tetraethyl orthosilicate (TEOS) and magnesium nitrate hexahydrate (MNH) as silicon and magnesium sources, respectively and by the addition of diluted nitric acid.

Nitric acid plays a role in the preparation of forsterite, as it regulates and lowers the pH. It also accelerates the hydrolysis and condensation processes of the dissolved compounds in liquid form, which helps in forming a highly homogeneous gel network. The presence of nitric acid ensures the oxidation of organic groups, such as residual solvents and alcohols, thereby reducing the remaining carbon and leading to higher crystalline purity after calcination. The controlled acidic medium promotes the homogeneous reaction of Mg^{2+} with SiO_2 and limits the formation of secondary phases such as MgO or free silica.

We prepared forsterite powder using the sol–gel method, in which magnesium nitrate was dissolved in distilled water and TEOS in ethanol. The mass of hydrated magnesium nitrate and TEOS were measured, and the volumes of ethanol and nitric acid were selected according to the ratios given in Table 1. The two precursor solutions were mixed under distillation with continuous magnetic stirring, followed by the addition of diluted nitric acid (HNO_3, 0.15 M) for two hours until a homogeneous transparent solution was obtained. This solution was then placed in a drying oven at 60 °C for 24 h to allow gel formation, and subsequently dried at 120 °C for 6 h. Finally, a yellowish oily powder was obtained.

Table 1 Ratios of hydrated magnesium nitrate and TEOS, and the volumes of ethanol and nitric acid

V_{HNO3}	V_{Eth}	V_{H2O}	V(TEOS) (ml)	M(NMg) (g)	Composite
$V_{HNO3} = 0636$ V_{TEOS}	$V_{Eth} = 1576$ V_{TEOS}	$V_{eau} = 3{,}1223$ V_{TEOS}	225.545	512.806	Mg_2SiO_4

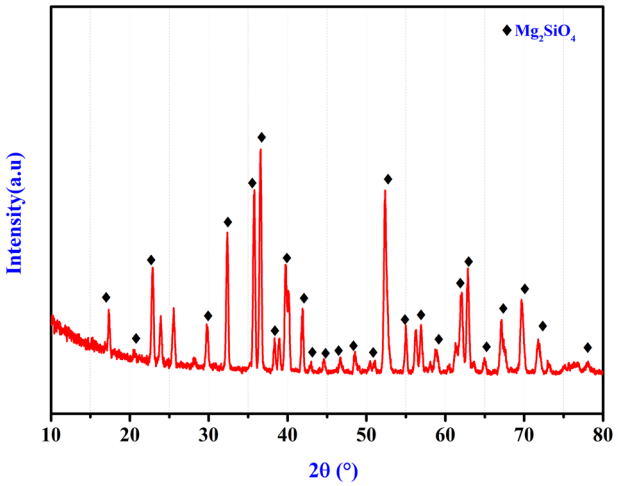

Fig. 2 XRD pattern of forsterite nanopowder (Mg_2SiO_4) sintered at 1450 °C for 2

This powder was manually ground with a mortar and pestle to break aggregates, then uniaxially cold-pressed into pellets. Finally, the samples were calcined and sintered at 1450 °C for 2 h to crystallize the forsterite phase and achieve densification. This optimized protocol ensures phase purity and controlled microstructure, critical for tailoring the material's electrical and mechanical properties.

2.3 Characterization and analysis

The structural and functional properties of the sintered forsterite pellets were systematically investigated using advanced analytical techniques. Phase purity and crystallinity were assessed via X-ray diffraction (XRD) using a PANalytical X'Pert Pro diffractometer with $Cu_{K\alpha}$ radiation ($\lambda = 1.5418$ Å), providing high-resolution data for Rietveld refinement. Microstructural analysis was performed using a QUANTA 250 FEG-FEI field emission scanning electron microscope (FESEM), equipped with energy-dispersive spectroscopy (EDS) to verify elemental homogeneity and grain morphology. For dielectric studies, pellets (~12 mm diameter × 1.5 mm thickness) were coated with silver electrodes and analyzed using Wayne Kerr 6500 P RLC meter across a broad frequency range (0.1 kHz–1 MHz) and temperatures (40–400 °C). These measurements revealed critical insights into the frequency-dependent conductivity, relaxation mechanisms, and electric modulus behavior, elucidating the roles of grain boundaries and defect dynamics in charge transport.

3 Results and discussion

3.1 XRD analysis

In order to confirm the phase purity of the prepared forsterite sample, the XRD pattern of forsterite nanopowder (Mg_2SiO_4) sintered at 1450 °C for 2 h is presented in Fig. 2, which shows reflections exclusively corresponding to the forsterite phase. The Rietveld XRD structural refinement of the heat-treated sample, displayed in Fig. 3, compares calculated intensities (solid lines) with empirical data (crosses), with the difference between the two plotted above the profile. The Bragg positions of forsterite are marked, and the results reveal excellent agreement between the calculated and experimental data, confirming the accuracy of the structural model and refinement parameters [20, 21]. The Rietveld analysis further confirms that the forsterite nanopowder exhibits an orthorhombic structure belonging to the space group *Pbnm*, with no secondary phases detected. The low reliability values achieved indicate that the proposed model accurately matches the experimental XRD pattern, validating the phase purity and structural integrity of the synthesized forsterite.

Figure 4 displays the final Rietveld refinement plot of the forsterite nanopowder (Mg_2SiO_4), illustrating the (001) projection of the unit cell derived from the crystallographic information file (CIF). This visualization provides a clear representation of the atomic arrangement within the forsterite structure. Table 2 summarizes the structural data obtained from the analysis, including lattice parameters, atomic positions, and other crystallographic details. The structural refinement was conducted using the Profex program in conjunction with Vesta software [22], which facilitated the accurate modeling and visualization of the forsterite crystal structure. The results demonstrate the precision of the refinement process, confirming the orthorhombic structure of forsterite and providing detailed insights into its crystallographic properties. An orthorhombic structure with a clearly defined cation distribution is where forsterite crystallizes.

Mg^{2+} are found in two different octahedral sites (M1 and M2), the M1 site is smaller and slightly more distorted, and the M2 site is larger, making it more tolerant to bigger cations, Si^{4+} ions are restricted to tetrahedral sites coordinated with oxygen. This collaborative approach between Profex and Vesta ensured a comprehensive and reliable

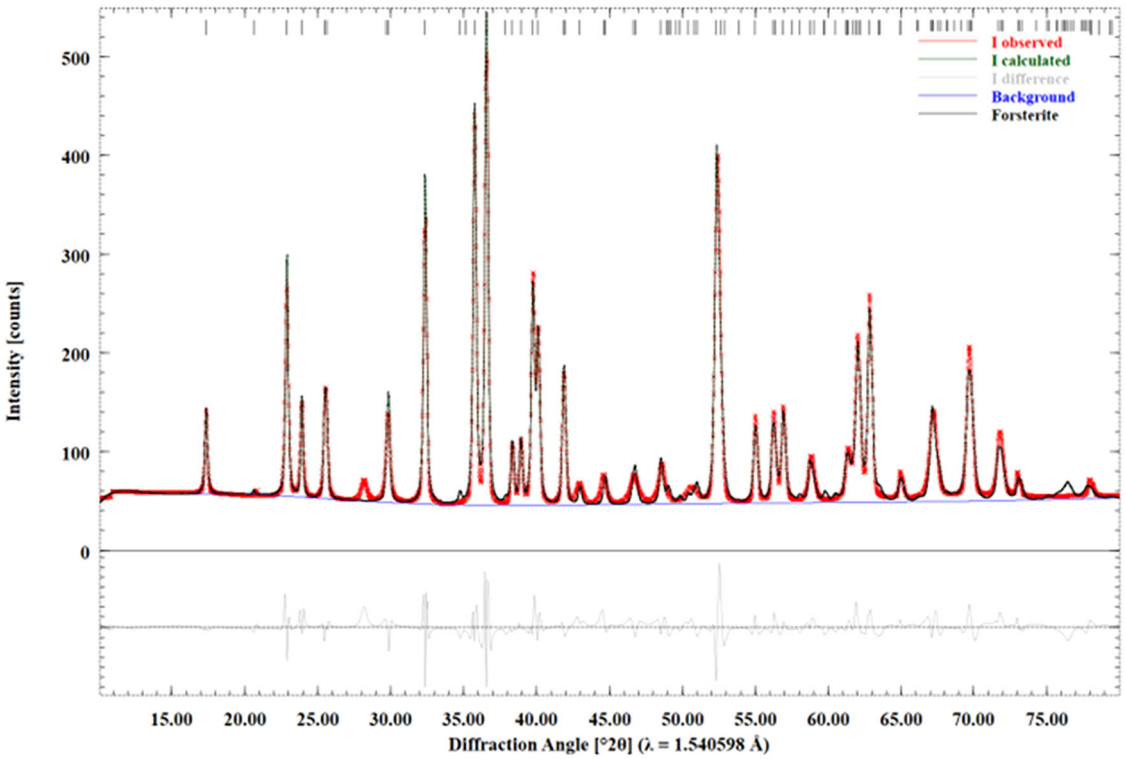

Fig. 3 The structural features of the Forsterite sample analyzed by the Rietveld refinement method

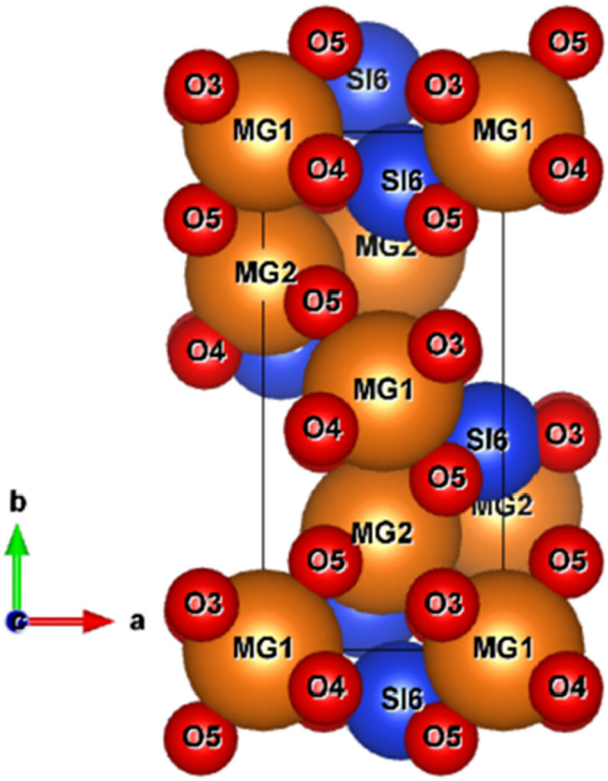

Fig. 4 Unit cell's (001) projection of the Forsterite sample

Table 2 The refined structural parameters obtained from the Rietveld analysis of the Forsterite sample

Phase Formula	Forsterite # Mg_2SiO_4					
Crystalline size/nm	25.34					
Lattice parameters	Space group: P b n m, a = 4.74779 ± −0.00045 (Å); b = 10.20328 ± 0. 00074 (Å); c = 5.98151 ± 0.00044 (Å); α = β = γ = 90∘; V = 289.762485 $Å^3$					
Reliability factors	Rwp = 7.83%; Rexp = 11.36%; χ2 = 0.4751					
	x	y	z	B	Occupancy	Site
Mg (1)	0.00000	0.00000	0.00000	0.993	1	4a
Mg (2)	0.99070	0.27619	0.25000	1.950	1	4c
O (3)	0.74710	0.08670	0.25000	7.873	1	4c
O (4)	0.24200	0.42750	0.25000	1.439	1	4c
O (5)	0.25960	0.17040	0.01710	1.715	1	8d
Si (6)	0.42730	0.09764	0.25000	1.216	1	4c
Refined chemical composition						
	Forsterite					
Phase quantity (wt-%)	100					

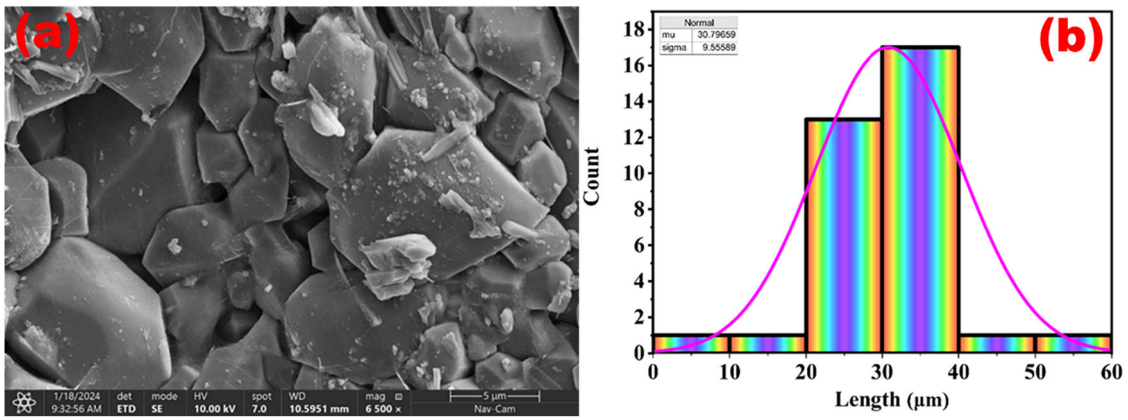

Fig. 5 Diagrams of **a** SEM micrograph and **b** distribution histogram of grains for forsterite sintered at 1450 °C for 2 h

Table 3 Values of density ρ (g/cm^3) open porosity (%), and relative density (%) of forsterite sintered at 1450 °C for 2 h

ρ	Open porosity	Relative density
2.5593	16.9935	78.2652

structural analysis, highlighting the phase purity and structural integrity of the synthesized forsterite nanopowder.

3.2 Microstructure, apparent porosity, and bulk density analysis

The SEM micrographs of forsterite pellets sintered at 1450 °C for 2 h, presented in Fig. 5, reveal a well-defined microstructure characterized by distinct grains separated by grain boundaries. The images depict a dense arrangement of forsterite granules with varying shapes and sizes, indicating a heterogeneous morphology. Notably, many of these granules exhibit a porous structure, which suggests the presence of interstitial voids or gaps within the material. This porous morphology is likely a result of the sintering process, where high temperatures facilitate grain growth and densification while leaving behind residual porosity. Figure 5b depicts the grain count plotted against particle size (µm). The particle size distribution, obtained through ImageJ software, closely followed a Lorentzian fitting curve. Based on SEM analysis, the average grain size was determined to be 30 µm sintered samples .

We employed the Archimedes method, which is based on the following equations [15, 20], to measure the density ρ (g/cm^3), open porosity (%), and relative density of the sintered forsterite (Mg_2SiO_4) samples at 1450 °C for two hours. The values of density ρ (g/cm^3), open porosity (%), and relative density (%) of forsterite sintered at 1450 °C for 2 h, are illustrated in Table 3.

3.3 EDS analysis

Figure 6 presents the EDS analysis of forsterite sintered at 1450 °C for 2 h, confirming the presence of its constituent elements through intense peaks corresponding to silicon (Si), magnesium (Mg), and oxygen (O). The atomic and weight percentages of these elements, align closely with the expected stoichiometric composition of forsterite (Mg_2SiO_4), demonstrating a high level of agreement with the theoretical values and validating the synthesis process. Figure 7 shows the corresponding EDS elemental maps, which reveal a homogeneous distribution of Mg, Si, and O across the sample without any significant agglomeration. This uniform distribution of elements within the grains further confirms the phase purity and compositional consistency of the synthesized forsterite, highlighting the successful preparation of the material under the given sintering conditions.

3.4 Impedance analysis

Complex impedance spectroscopy was employed to study the electrical behavior of forsterite nanopowder samples synthesized via the sol–gel method and sintered at 1450 °C. Figure 8a illustrates the variation of the real part of impedance (Z″) for the forsterite nanopowder across a frequency range of 10^2–10^6 Hz at different temperatures (40, 100, 200, 300, and 400 °C). The results show that the real part of impedance (Z″) decreases with increasing temperature and frequency, indicating a rise in AC conductivity [23, 24]. At lower frequencies, the decrease in Z' with increasing temperature aligns with the behavior observed in ceramics [25], bioceramics [26], PZT [27], and semiconductors [28], suggesting thermally activated conduction mechanisms. At higher frequencies, the values of Z' converge and become frequency-independent for all temperatures, a phenomenon attributed to the release of

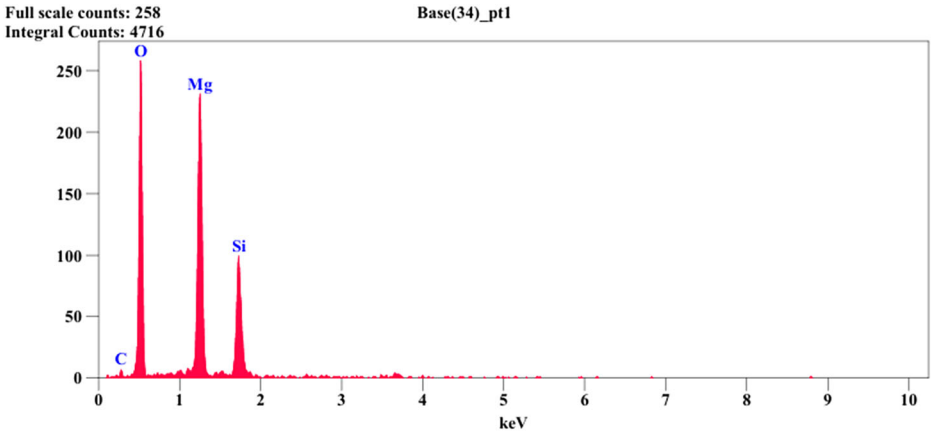

Fig. 6 EDS profile of forsterite sintered at 1450 °C for 2 h

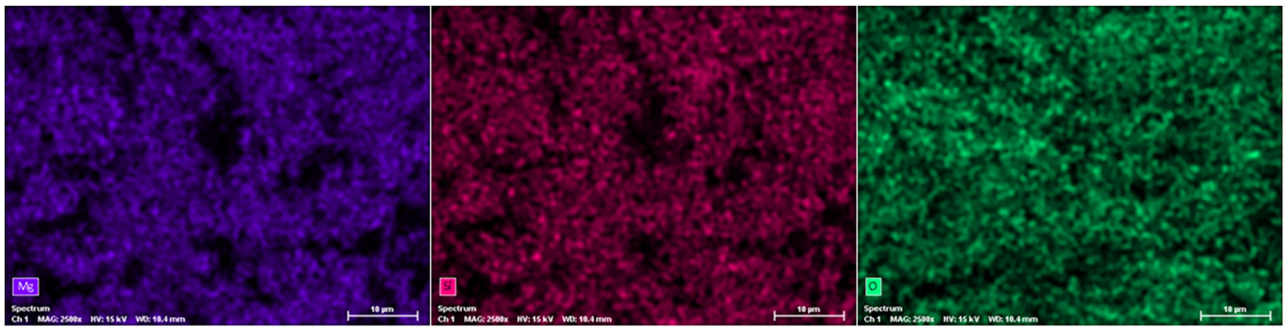

Fig. 7 EDS elemental mapping of forsterite sintered at 1450 °C for 2 h

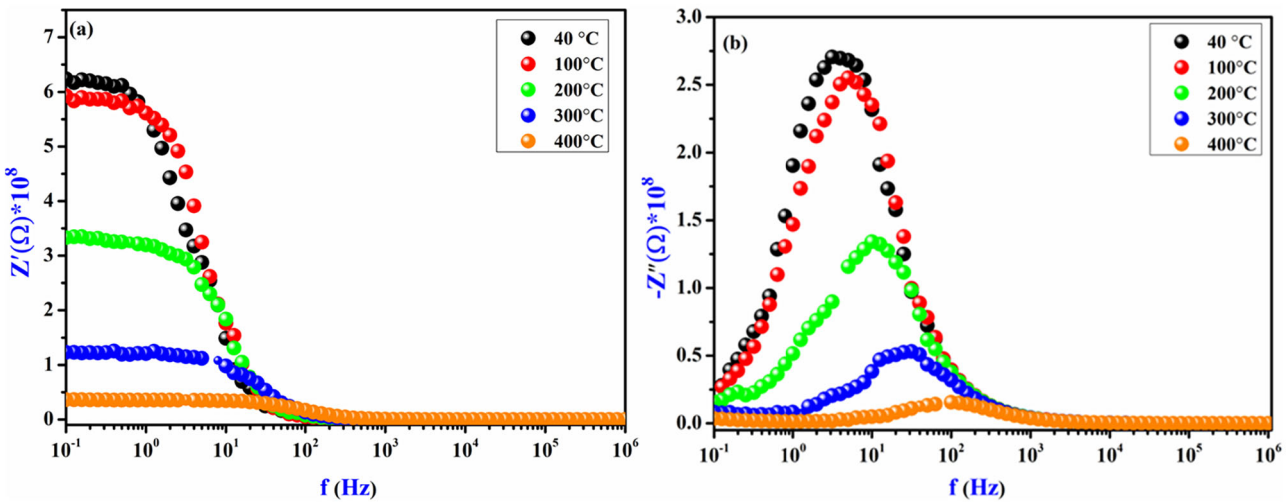

Fig. 8 Dependence of **a** the real component of impedance (Z') and **b** the negative imaginary component (-Z") on frequency at varying temperatures for the forsterite sample

space charges due to the reduced barrier properties of the material [29].

Figure 8b depicts the frequency-dependent variation of the imaginary part of the impedance (-Z″) for the forsterite nanopowder at different temperatures. A broad and asymmetrical peak is observed at all temperatures, indicating the presence of relaxation processes within the material. As the frequency increases, the values of -Z″ rise, reaching a maximum value ($-Z''_{max}$), before subsequently decreasing. This behavior is characteristic of dielectric relaxation, where the relaxation time is influenced by temperature. Notably, the peak position ($-Z''_{max}$) shifts to higher frequencies as the temperature increases, reflecting a reduction in relaxation time with rising temperature [30, 31]. This temperature-

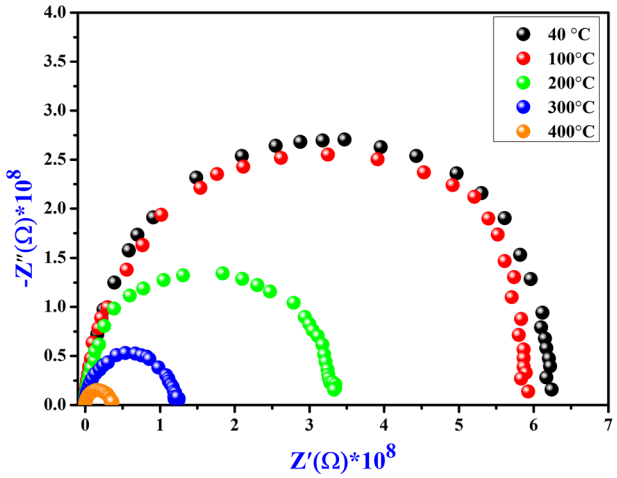

Fig. 9 Nyquist plot of the forsterite sample at different temperatures

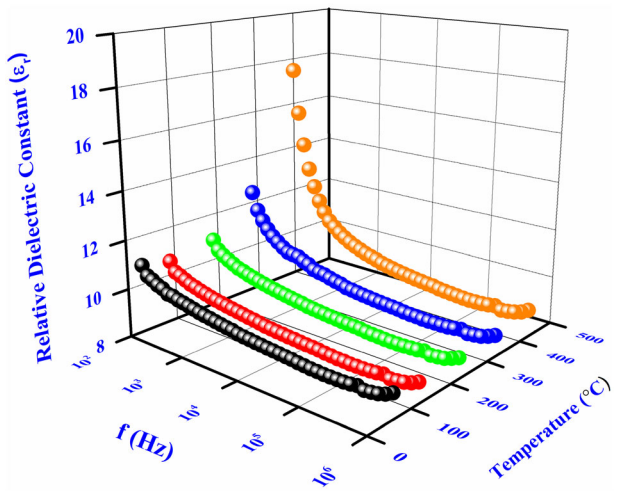

Fig. 10 The dependence of dielectric permittivity (ε_r) on frequency at various temperatures for the forsterite sample

dependent shift suggests that the relaxation mechanisms in the forsterite nanopowder are thermally activated, consistent with typical behavior observed in dielectric materials.

Figure 9 presents typical Nyquist plots (complex impedance spectra) for the forsterite sample sintered at 1450 °C for 2 h, measured at various temperatures (40, 100, 200, 300, and 400 °C). The plots exhibit a single semicircular arc, the radius of which decreases with increasing temperature. This reduction in arc radius is attributed to the presence of electrical relaxation processes, indicating non-Debye type behavior in the forsterite sample [32, 33]. The observed temperature dependence highlights the influence of thermal activation on the material's electrical properties. The presence of a single semicircular arc suggests that the electrical response is primarily dominated by the grain contribution, with minimal influence from grain boundaries or other interfaces [33–35].

3.5 Dielectric analysis

The dielectric behavior of a solid material is often characterized by the dielectric permittivity (ε_r), which quantifies the material's ability to store electrical energy in an electric field. The relative dielectric constant (ε_r) can be calculated from capacitance measurements using the formula [36]:

$$\varepsilon_r = C\frac{d}{A\varepsilon_0} \tag{1}$$

where C is the capacitance, d is the thickness of the sample, A is the area of the electrode, and ε_o is the permittivity of free space 8.854×10^{-12} F/m.

Dielectric permittivity (ε_r) of forsterite pellets sintered at 1450 °C for 2 h (The dielectric properties were investigated in the current work using a sintering temperature of 1450 °C since it produces higher condensation) was evaluated, as shown in Fig. 10, which illustrates the frequency-dependent spectra of ε_r within the range of 10^2–10^6 Hz at temperatures from to 40 °C to 400 °C in 100 °C increments. The results reveal that ε_r decreases with increasing frequency, while it increases with rising temperature. This behavior can be attributed to the combined contributions of various polarization mechanisms, including atomic, ionic, and electronic polarization [37–40]. At lower frequencies, these polarization mechanisms are more active, leading to higher ε_r values, but as frequency increases, the inability of dipoles to align with the rapidly alternating electric field causes ε_r to drop significantly [37–39]. At high frequencies, ε_r stabilizes due to the dominance of interfacial polarization [40, 41]. The relatively low dielectric permittivity of forsterite makes it a promising candidate for applications in multifunctional substrates and electronic components, where materials with stable and low dielectric properties are essential [42]. The obtained values of dielectric permittivity for forsterite pellets sintered at 1450 °C for 2 h are higher than those reported in [7, 8]. This enhancement can be attributed to several factors: the influence of the majority phases (such as mullite) and their proportions, the effect of processing conditions and porosity on dielectric behavior [23], and the use of a sintering temperature of 1450 °C for two hours, which promotes higher condensation and densification. In addition, microstructural features including agglomeration, particle size distribution, crystallite size, and porosity played a significant role in determining the dielectric permittivity values obtained in the present study.

The real (ε') and imaginary (ε'') components of the dielectric permittivity are derived from complex impedance data using the following relationships [43–45]:

$$\varepsilon' = -\frac{Z''}{\omega * C_0\left(Z''^2 + Z'^2\right)} \tag{2}$$

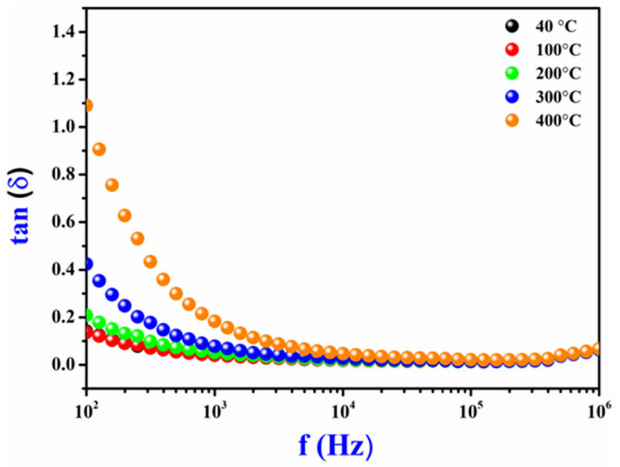

Fig. 11 The dependence of the loss tangent tan(δ) on frequency at various temperatures for the forsterite sample

$$\varepsilon'' = \frac{Z'}{\omega * C_0\left(Z''^2 + Z'^2\right)} \tag{3}$$

Here, Z' and Z'' are the real and imaginary parts of the impedance, ω is the angular frequency ($\omega = 2\pi f$), and C_0 is the geometrical capacitance of the sample. Moreover, the loss tangent (tan(δ)), a measure of energy dissipation in a dielectric material, can be calculated from complex impedance data using the equation [43]:

$$\tan\delta = \frac{\varepsilon'}{\varepsilon''} \tag{4}$$

Figure 11 illustrates the frequency dependence of the loss tangent (tan(δ)) for forsterite pellets sintered at 1450 °C for 2 h, measured at temperatures ranging from 40 to 400 °C. The results show that tan δ decreases with increasing frequency at a constant temperature, while it increases with rising temperature at a constant frequency. This behavior can be attributed to the influence of DC conduction at low and intermediate frequencies, where higher temperatures enhance ionic mobility and conductivity, leading to increased energy losses and higher tan (δ) values. As the frequency increases, the dipoles become less able to follow the rapidly alternating electric field, resulting in reduced energy dissipation and lower tan (δ). The observed trends align with previous studies [45], confirming the temperature and frequency dependence of dielectric losses in forsterite. These findings highlight the material's dielectric behavior and its implications for applications in high-temperature electronic and insulating systems, where understanding energy loss mechanisms is critical.

Specifically, the low dielectric loss and observed dielectric permittivity in the measured region are indicative of intrinsic polarization mechanisms (ionic and electronic contributions …), which diminish with increasing frequency, whereas interfacial and dipolar relaxations remain active at higher frequencies. Thus, the low losses and steady dielectric response in the tested range point to promising higher frequency performance. Furthermore, similar ceramics reported in the literature have shown consistent dielectric behavior from low frequencies up to the GHz range, suggesting that our samples are likewise suitable for high-frequency applications.

In high-frequency communications, low permittivity $\varepsilon_r < 10$ and low loss (high-quality factor) are both necessary because of the high data transmission rate that can only be attained by low-time delay signal transmission [38].

The relationship between the relative permittivity (ε_r) and the time delay in a resonator is as follows [38]:

$$t_d = l\sqrt{\frac{\varepsilon_r}{C}} \tag{5}$$

where L: represents the signal transmission distance, C: represents the velocity of light, and (ε_r): is the relative permittivity.

3.6 Electrical modulus spectroscopy

Electrical modulus spectroscopy is a powerful technique for investigating polarization mechanisms and relaxation processes in materials, particularly those arising from electrode effects, grain, and grain boundary contributions. The complex electrical modulus (M*), which consists of a real part (M′) and an imaginary part (M″), is defined by the equation [46–48]:

$$M^* = M' + jM'' \tag{6}$$

The real part (M′) and imaginary part (M″) of the electrical modulus can be calculated using the dielectric constants ε‘ and ε“ through the relationships:

$$M' = \frac{\varepsilon'}{\left(\varepsilon'^2 + \varepsilon''^2\right)} \tag{7}$$

$$M'' = \frac{\varepsilon''}{\left(\varepsilon'^2 + \varepsilon''^2\right)} \tag{8}$$

These equations transform the dielectric data into the modulus formalism, which helps to isolate and analyze the relaxation processes related to conductivity and interfacial effects.

Figure 12 illustrates the frequency dependence of the real part of the electric modulus (M') for forsterite nanopowder sintered at 1450 °C for 2 h, measured at various temperatures. At lower frequencies, M' approaches zero, indicating that electrode polarization effects are negligible and do not significantly influence the material's electrical response.

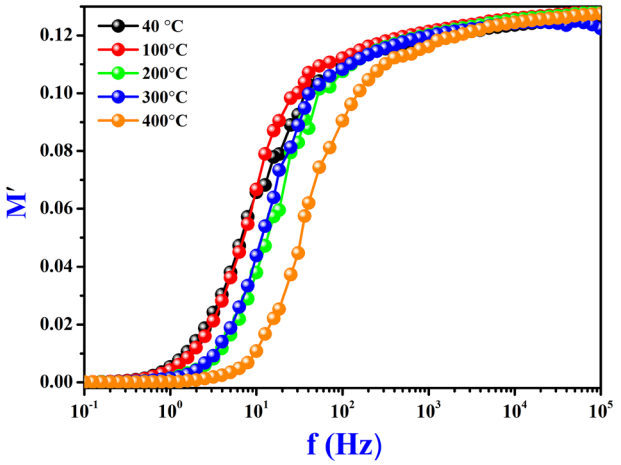

Fig. 12 Variation of the real part of the electric modulus (M') with frequency at various temperatures for the forsterite sample

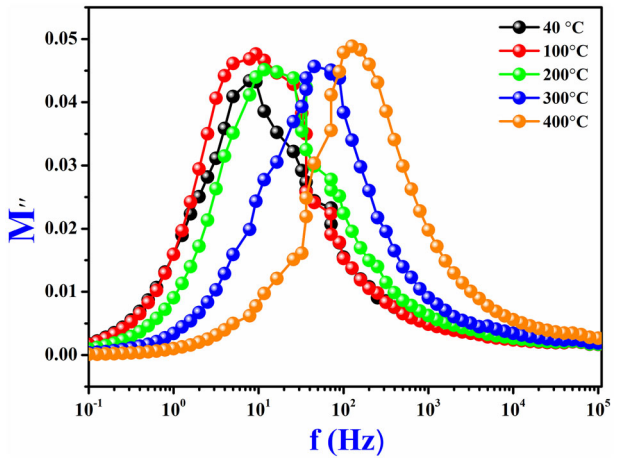

Fig. 13 The variation in the imaginary part of the electric modulus (M") with frequency at various temperatures for the forsterite sample

However, at higher frequencies, M' reaches a maximum value, suggesting the presence of conductivity relaxation processes [49, 50]. The dispersion observed between these frequency ranges is attributed to the transition of charge carriers over short distances, which becomes restricted as frequency increases [51, 52]. This behavior highlights the material's frequency-dependent dielectric properties and provides insights into the mechanisms governing charge transport and relaxation.

Figure 13 shows the variation of the imaginary part of the electric modulus (M") with frequency at different temperatures for forsterite nanopowder sintered at 1450 °C for 2 h. The plot reveals a relaxation peak that shifts to higher frequencies as the temperature increases, indicating temperature-dependent relaxation processes. The asymmetric broadening of the relaxation peak suggests a distribution of relaxation times with multiple time constants, characteristic of non-Debye type relaxation behavior

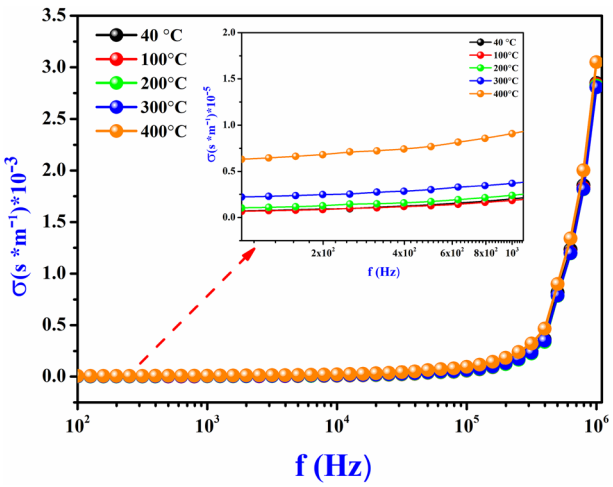

Fig. 14 The variation of electrical conductivity with frequency at different temperatures for the forsterite sample

[20, 21, 49, 50]. This non-ideal behavior implies that the relaxation mechanisms in the forsterite sample are influenced by a combination of factors, such as grain boundaries, defects, or localized charge carrier movements, rather than a single dominant process.

3.7 Electrical conductivity

To analyze the electrical conductivity behavior of forsterite nanopowder sintered at 1450 °C for 2 h, impedance spectroscopy measurements were used to calculate the conductivity across a frequency range of 10^2–10^6 Hz at various temperatures (40, 100, 200, 300, and 400 °C). The electrical conductivity (σ) was determined using the equation [43]:

$$\sigma = \frac{t}{A}\frac{(Z')}{\left(Z''^2 + Z'^2\right)} \tag{9}$$

where A and t represent the area and thickness of the pellet.

Figure 14 illustrates the frequency-dependent electrical conductivity behavior of forsterite nanopowder sample, measured at various temperatures (40, 100, 200, 300, and 400 °C). The conductivity exhibits two distinct regions: at lower frequencies, the conductivity remains relatively constant, forming a plateau that corresponds to the direct current conductivity (σ_{dc}) of the material [43], which is primarily governed by long-range charge transport mechanisms. At higher frequencies, beyond the plateau region, the conductivity ($\sigma_a c$) increases with frequency, indicating a shift in the conduction mechanism. This frequency-dependent behavior is attributed to the activation of localized charge carriers and polarization effects, which dominate at higher frequencies [53, 54]. The observed trends highlight the transition from long-range DC conduction to short-range AC conduction, providing important

understandings of the charge transport dynamics and conduction mechanisms in forsterite nanopowder, which are critical for its potential applications in electronic and dielectric systems.

Jonscher's law provides a widely accepted interpretation for the frequency-dependent conductivity dispersion observed in materials, including forsterite, particularly at high frequencies [33, 43]. According to this law, the total electrical conductivity (σ) can be expressed as [33]:

$$\sigma = \sigma_{dc} + A\omega^{s} \tag{10}$$

where σ_{dc} represents the temperature-dependent DC conductivity at low frequencies, ω is the angular frequency, A is a temperature-dependent coefficient, and s is the frequency exponent that reflects the degree of interaction between mobile charge carriers and their surrounding lattice [33]. The term $A\omega^{s}$ accounts for the increase in conductivity at higher frequencies, which arises from localized charge carrier movements and polarization effects. The exponent s typically ranges between 0 and 1, with lower values indicating stronger interactions and correlated hopping mechanisms. Jonscher's law effectively explains the transition from frequency-independent DC conductivity (σ_{dc}) at low frequencies to frequency-dependent AC conductivity ($A\omega^{s}$) at high frequencies, offering a comprehensive framework for understanding the conduction mechanisms in forsterite and other dielectric materials. The frequency exponent (s) exhibited values of 1.85, 1.85, 1.83, and 1.76 at 100, 200, 300, and 400 °C, respectively, for the forsterite sample, indicating a conduction mechanism that deviates from classical hopping models where $s \leq 1$. These unusually high s-values (>1) suggest the dominance of correlated barrier hopping (CBH) or polaron-assisted conduction, where strong charge carrier-lattice interactions lead to enhanced frequency-dependent conductivity. The slight decrease in s with increasing temperature implies reduced charge localization at higher temperatures, as thermal energy facilitates more delocalized transport. This behavior aligns with Maxwell–Wagner interfacial polarization effects and non-Debye relaxation processes, commonly observed in ceramics with mixed ionic-electronic conduction. The observed trends reflect the complex interplay between defect-assisted hopping, grain boundary contributions, and thermally activated conduction mechanisms in forsterite, consistent with its role as a high-temperature dielectric material.

To determine the activation energy (E_a) of the forsterite nanopowder, the DC conductivity (σ_{dc}) measured at low frequencies was analyzed using the Arrhenius equation [33]:

$$\sigma_{dc} = \sigma_0 \exp\left(\frac{-E_a}{k_B T}\right) \tag{11}$$

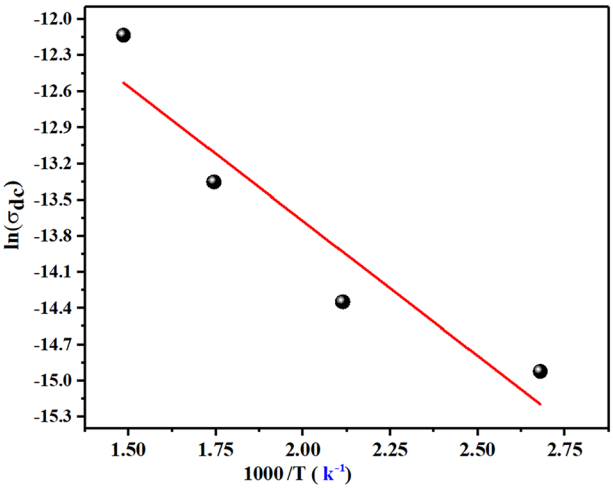

Fig. 15 The plot of ln (σ_{dc}) versus 1000/T for forsterite sample

where σ_0 is the pre-exponential factor representing intrinsic conductivity, k_B is the Boltzmann constant, and T is the absolute temperature [33]. This equation describes the thermally activated behavior of charge transport, where the conductivity increases exponentially with temperature. The activation energy (E_a) represents the energy barrier that charge carriers must overcome to contribute to conduction, providing insights into the dominant conduction mechanism (e.g., ionic or electronic). By plotting $\ln(\sigma_{dc})$ versus 1000/T in Fig. 15, E_a is derived from the slope of the linear fit.

The activation energy (E_a) for forsterite sintered at 1450 °C for 2 h is determined to be 0.19 eV, which aligns well with the previously reported value in reference [33]. This consistency suggests that the conduction mechanism in the sample studied follows a similar thermal activation process as observed in prior research.

4 Conclusions

The current work successfully demonstrated the synthesis of high-performance forsterite (Mg_2SiO_4) ceramics via a controlled sol–gel process. The phase-pure orthorhombic structure (*Pbnm* space group) and stoichiometric composition (Mg:Si:O ≈ 2:1:4) confirmed by XRD and EDS. The exceptional dielectric properties low permittivity ($\varepsilon_r \sim 9.12$ at 1 MHz) and minimal losses ($\tan\delta < 0.015$) coupled with frequency-stable conductivity, make forsterite ideal for high-frequency applications such as 5 G substrates or satellite communications. The observed correlated barrier hopping (CBH) conduction (exponent $s = 1.85$–1.76) and low activation energy ($E_a = 0.19$ eV) reveal polaron-assisted transport, highlighting the material's unique charge dynamics. Non-Debye relaxation behavior further

emphasizes the role of grain boundaries in modulating electrical response. These findings not only advance the fundamental understanding of forsterite's structure-property relationships but also pave the way for its deployment in next-generation electronics, biomedical implants, and refractory systems.

Data availability

No datasets were generated or analysed during the current study.

Author contributions AK; methodology, planned and conducted the tests, prepared the manuscript, revised and validated the final manuscript, MH, data analysis and interpretation, prepared the manuscript, revised and validated the final manuscript, LA; data analysis and interpretation, prepared the manuscript, revised and validated the final manuscript, TAMT; prepared the manuscript, revised and validated the final manuscript, RM; prepared the manuscript, revised and validated the final manuscript. All authors have read and approved the final manuscript version.

Compliance with ethical standards

Conflict of interest The authors declare no competing interests.

References

1. Rana A, Kumar V, Awasthi AM (2021) Effect of dopant concentration and annealing temperature on electric and magnetic properties of lanthanum substituted $CoFe_2O_4$ nanoparticles for potential use in 5G wireless communication systems. Ceramics Int 47(14):20669–20677. https://doi.org/10.1016/j.ceramint.2021.04.077
2. Dinesh MA, Kumar R, Gupta VR, Dayal V (2025) Synthesis, characterization, and application of $Ba_3V_2O_8$ ceramics in cylindrical dielectric resonator antenna: Simulation and experimental study. Materials Sci Eng B 311:117791
3. Keziz A, Heraiz M, Sahnoune F, Rasheed M (2023) Characterization and mechanisms of the phase's formation evolution in sol-gel derived mullite/cordierite composite. Ceramics Int 49(20):32989–33003. https://doi.org/10.1016/j.ceramint.2023.09.068
4. Asghar G, Dong X, Chae S, Yoo CS, Jeon J, Woo C, Choi JY (2023) Dielectric properties of low-temperature sintered forsterite (Mg_2SiO_4) using high-dispersion and nanoparticle-based solid-state reaction process. Materials Lett 337:134009. https://doi.org/10.1016/j.matlet.2023.134009
5. Asghar G, Dong X, Chae S, Yoo C-S, Oh S, Choi KH, Jeon J, Woo C, Kim TY, Ahn J (2022) Synthesis of hollow forsterite by coating method and study of its dielectric properties. Ceram Int https://doi.org/10.1016/j.ceramint.2022.09.372
6. Keshavarz M, Ebadzadeh T, Banijamali S (2017) Preparation of forsterite/MBS (MgO-B_2O_3-SiO_2) glass-ceramic composites via conventional and microwave assisted sintering routes for LTCC application. Ceramics Int 43(12):9259–9266. https://doi.org/10.1016/j.ceramint.2017.04.082
7. Dong H, Liang Y, Nie J, Cai M, Ju M, Li Z, Zhou Y (2023) Synthesis of forsterite with high strength and low acid solubility using magnesite tailings. Ceramics Int 49(8):13258–13264. https://doi.org/10.1016/j.ceramint.2023.01.066
8. Bafrooei HB, Ebadzadeh T, Majidian H (2014) Microwave synthesis and sintering of forsterite nanopowder produced by high energy ball milling. Ceram Int 40(2):2869–2876. https://doi.org/10.1016/j.ceramint.2013.10.025
9. Pratapa S, Handoko WD, Nurbaiti U (2017) Synthesis and characterization of high-density B_2O_3-added forsterite ceramics. Ceramics Int 43(9):7172–7176. https://doi.org/10.1016/j.ceramint.2017.03.002
10. Laziri K, Djemli A, Redaoui D, Sahnoune F, Dhahri E, Hassan SF, Saheb N (2024) Kinetics of formation, microstructure, and properties of monolithic forsterite (Mg_2SiO_4) produced through solid-state reaction of nano-powders of MgO and SiO_2. Ceramics Int 50(22):45179–45188. https://doi.org/10.1016/j.ceramint.2024.08.357
11. Mohagheghiyan K, Mokhtari H, Kharaziha M (2024) Gelatin-coated mesoporous forsterite scaffold for bone tissue engineering. Ceramics Int 50(8):13526–13535. https://doi.org/10.1016/j.ceramint.2024.01.266
12. Soleimani F, Dehghani P (2024) Production of dense forsterite with ultra low dielectric loss using ZrO_2 additive. Ceramics Int 50(18):32972–32977. https://doi.org/10.1016/j.ceramint.2024.06.111
13. Mirjalili F, Manafi S, Lotfi F (2020) Examination of morphology, degradation and biocompatibility of fluorapatite–forsterite nanocomposite. Ceramics Int 46(13):21256–21267. https://doi.org/10.1016/j.ceramint.2020.05.216
14. Liu Y, Liu P, Hu C (2018) Hydrothermally assisted synthesis of pure-phase and well-dispersed forsterite nanopowders. Ceramics Int 44(18):23339–23343. https://doi.org/10.1016/j.ceramint.2018.09.120
15. Keziz A, Heraiz M, Sahnoune F et al. (2023) Dense, hard, and thermally stable $Al_6Si_2O_{13}$–$Mg_2Al_4Si_5O_{18}$ composite material for silicon substrate applications. Silicon 15:4675–4688. https://doi.org/10.1007/s12633-023-02373-y
16. Ohsato H, Tsunooka T, Sugiyama T et al. (2006) Forsterite ceramics for millimeterwave dielectrics. J Electroceram 17:445–450. https://doi.org/10.1007/s10832-006-0452-6
17. Saberi A, Alinejad B, Negahdari Z, Kazemi F, Almasi A (2007) A novel method to low temperature synthesis of nanocrystalline forsterite. Mater Res Bull 42(4):666–673. https://doi.org/10.1016/j.materresbull.2006.07.020
18. Liu Y, Liu P, Hu C (2018) Hydrothermally assisted synthesis of pure-phase and well- dispersed forsterite nanopowders. Ceram Int 44(18):23339–23343. https://doi.org/10.1016/j.ceramint.2018.09.120
19. Temuujin J, Okada K, MacKenzie K (1998) Role of water in the mechanochemical reactions of MgO–SiO_2 systems. J Solid State Chem 138(1):169–177. https://doi.org/10.1006/jssc.1998.7768
20. Djelel K, Keziz A, Rasheed M, Oueslati A (2024) SiO_2's influence on the dielectric properties of natural fluorapatite-derived bio-compounds. Ceramics Int https://doi.org/10.1016/j.ceramint.2024.12.296
21. Keziz A, Heraiz M, Rasheed M, Oueslati A (2024) Investigating the dielectric characteristics, electrical conduction mechanisms, morphology, and structural features of mullite via sol-gel synthesis at low temperatures. Materials Chem Phys 325:129757. https://doi.org/10.1016/j.matchemphys.2024.129757
22. Ghelloudj E, Keziz A (2025) Experimental failure analysis of AISI 4140 steel interconnecting shaft of the high-speed centrifugal compressor for regeneration gas. Eng Fail Anal, 109283 https://doi.org/10.1016/j.engfailanal.2025.109283
23. Wan Y, Li X, Ma J (2023) Mullite porous ceramics with high strength for hightemperature thermal insulation. J Mater Sci Technol 27:5692–5700. https://doi.org/10.1016/j.jmrt.2023.10.288
24. Enneffati M, Louati B, Guidara K, Rasheed M, Barill R (2017) ´e, Crystal structure characterization and AC electrical conduction behavior of sodium cadmium orthophosphate. J Mater Sci Mater Electron 29(1):171–179. https://doi.org/10.1007/s10854-017-7901-7

25. Zhu J, Zhu R, Hu Y, Wang Z (2024) Mullite fiber porous ceramic with high quality factor for high-temperature PM filtration. J Eur Ceram Soc 44:2630–2637. https://doi.org/10.1016/j.jeurceramsoc.2023.11.064
26. Helen S, Saravanan L, Sabari V, Senthilkumar K, Kanagathara N (2023) Temperature- dependent dielectric investigation of dual-ions doped hydroxyapatite nanoparticles. Inorg Chem Commun 158:111606–111606. https://doi.org/10.1016/j.inoche.2023.111606
27. Peng Z-H, Zheng D-Y, Zhou T, Yang L, Zhang N, Fang C (2018) Effects of Co_2O_3 doping on electrical properties and dielectric relaxation of PMS–PNN–PZT ceramics. J Mater Sci Mater Electron 29(7):5961–5968. https://doi.org/10.1007/s10854-018-8569-3
28. Tihtih M, Ibrahim JEF, Basyooni MA, En-Nadir R, Belaid W, Hussainova I, Kocserha I (2023) Development of yttrium-doped $BaTiO_3$ for next-generation multilayer ceramic capacitors. ACS omega 8(9):8448–8460
29. Tihtih M, Ibrahim JEF, Basyooni MA, En-Nadir R, Hussainova I, Kocserha I (2023) Functionality and activity of sol–gel-prepared Co and Fe co-doped lead-free BTO for thermo-optical applications. ACS omega 8(5):5003–5016
30. Tihtih M, Ibrahim JEF, Basyooni MA, En-Nadir R, Belaid W, Hussainova I, Kocserha I (2023) Development of yttrium-doped $BaTiO_3$ for next-generation multilayer ceramic capacitors. ACS omega 8(9):84 48–8460
31. Mahani RM, Omara S (2019) Grain and grain boundaries contributions to dielectric relaxation of the clay-based ceramics. Appl Phys A 125(8):573
32. Chérif SF, Chérif A, Dridi W, Zid MF (2020) Ac conductivity, electric modulus analysis, dielectric behavior and Bond Valence Sum analysis of $Na_3Nb_4As_3O_{19}$ compound. Arab J Chem 13(6):5627–5638
33. El Asri S, El Hadri M, Rahim MA, Essaleh L, Ahamdane H, Hajji L, Mansori M (2022) Structural, microstructure and ac impedance spectroscopy investigation of parent and M-doped forsterite $Mg_{1.9}M_{0.1}SiO_4$ (M= Co, Ni and Mn). Phys B Condens Matter 643:414127. https://doi.org/10.1016/j.physb.2022.414127
34. Karbovnyk I, Borshchyshyn I, Vakhula Y, Lutsyuk I, Klym H, Bolesta I (2016) Impedance characterization of Cr^{3+}, Y^{3+} and Zr^{4+} activated forsterite nanoceramics synthesized by sol–gel method. Ceramics Int 42(7):8501–8504. https://doi.org/10.1016/j.ceramint.2016.02.075
35. Nouri F, Trabelsi-Ayadi M, Riadh Ternane (2022) Synthesis and ionic conductivity of phosphate-sulfate fluorapatites $Ca_{10-x}Nax(PO_4)_{6-x}(SO_4)_xF_2$(x = 0, 3, 6). Mater Sci Eng B 282:115786–115786. https://doi.org/10.1016/j.mseb.2022.115786
36. Benmakhlouf A, Makhloufi R, Boutarfaia A, Messai B, Hadji F, Nouiri M (2023) The effect of Barium substitution on the structural and dielectric properties of Pb1-XBaX $(Zr_{0.52}Ti_{0.43}(Al_{0.5}Sb_{0.5})_{0.05})O_3$ ceramics at the morphotropic phase boundary. J Ovonic Res 19(3):295–305
37. Kool A, Thakur P, Bagchi B, Hoque NA, Banerjee S, Das S (2015) Sol–gel synthesis of transition-metal ion conjugated alumina-rich mullite nanocomposites with potential mechanical, dielectric and photoluminescence properties. RSC Adv 5(126):104299–104313
38. Keziz A, Rasheed M, Heraiz M, Sahnoune F, Latif A (2023) Structural, morphological, dielectric properties, impedance spectroscopy and electrical modulus of sintered $Al_6Si_2O_{13}$–$Mg_2Al_4Si_5O_{18}$ composite for electronic applications. Ceramics Int 49(23):37423–37434. https://doi.org/10.1016/j.ceramint.2023.09.068
39. Kool A, Thakur P, Bagchi B, Hoque NA, Das S (2015) Mechanical, dielectric and photoluminescence properties of alumina–mullite composite derived from natural Ganges clay. Appl Clay Sci 114:349–358
40. Belhouchet K, Bayadi A, Belhouchet H, Romero M (2019) Improvement of mechanical and dielectric properties of porcelain insulators using economic raw materials. Bol Soc Espanola Ceram Vidr 58(1):28–37
41. Carvalho RS, Da Silva VJ, Da N´obrega RB, Lira HL, Santana LNL (2019) Fabrication and characterization of dielectric ceramics using alumina and aluminosilicates. Cerˆamica 66:56–64
42. Synkiewicz-Musialska B, Szwagierczak D, Kulawik J, Pałka N, Piasecki P (2021) Structural, thermal and dielectric properties of low dielectric permittivity cordierite-mullite-glass substrates at terahertz frequencies. Materials 14(14):4030
43. Messai B, Makhloufi R, Keziz A, Benmakhlouf A, Nouiri M, Taha TAM (2025) Integrated study of morphology, structure, and dielectric behavior in PZT-SASF ceramics at the morphotropic phase boundary. Ceramics Int https://doi.org/10.1016/j.ceramint.2025.01.496
44. Deka B, Ravi S, Pamu D (2017) Impedance spectroscopy and ac conductivity mechanism in Sm doped Yttrium Iron Garnet. Ceramics Int 43(13):10468–10477. https://doi.org/10.1016/j.ceramint.2017.05.089
45. Kherifi D, Keziz A, Rasheed M, Oueslati A (2024) Thermal treatment effects on Algerian natural phosphate bioceramics: a comprehensive analysis. Ceramics Int https://doi.org/10.1016/j.ceramint.2024.05.317
46. Rout A, Agrawal S (2021) Investigation of electrical conduction in $Ca_{6-x}Na_2Y_2$ $(SiO_4)_6F_2$:xEu^{3+} ceramic by complex impedance and electric modulus spectroscopy. Ceramics Int 47(5):7032–7044. https://doi.org/10.1016/j.ceramint.2020.11.053
47. Aslam S, Shifa MS, Gilani ZA, Usmani MN, Rehman JU, Khan MA, Khalid M (2019) Structural, optical and magnetic elucidation of co-doping of Nd^{3+} and Pr^{3+} on lithium nanoferrite and its technological application. Results Phys 12:1334–1339. https://doi.org/10.1016/j.rinp.2019.01.018
48. Khan JK, Khalid M, Chandio AD, Shahzadi K, Uddin Z, Mustafa G, Gilani ZA (2022) Properties of Al^{3+} substituted nickel ferrite ($NiAl_xFe_{2-x}O_4$) nanoparticles synthesised using wet sol-gel auto-combustion. J Sol Gel Sci Technol 101(3):606–617. https://doi.org/10.1007/s10971-020-05426-5
49. Warsi MF, Gilani ZA, Al-Khalli NF, Sarfraz M, Khan MA, Anjum MN, Shakir I (2017) New $LiNi_{0.5}Pr_xFe_{2-x}O_4$ nanocrystallites: Synthesis via low cost route for fabrication of smart advanced technological devices. Ceramics Int 43(17):14807–14812. https://doi.org/10.1016/j.ceramint.2017.07.228
50. Gilani ZA, Shifa MS, Khan MA, Anjum MN, Usmani MN, Ali R, Warsi MF (2018) New $LiCo_{0.5}PrxFe_{2-x}O_4$ nanoferrites: prepared via low cost technique for high density storage application. Ceramics Int 44(2):1881–1885. https://doi.org/10.1016/j.ceramint.2017.10.126
51. Parveen A, Asghar HNUHK, Khalid M, Gilani ZA, Aslam S, Saleem M, Rehman J (2019) Dielectric, impedance and modulus spectroscopic studies of $Co_{0.3}Cd_{0.7}Zn1.$ $5_xFe_{2-x}O_4$ nanoparticles. Applied Phys A 125(10):731
52. Mustaqeem M, Mahmood K, Saleh TA, ur Rehman A, Ahmad M, Gilani ZA, Asif M (2020) Synthesis of $CuFe_{2-x}Er_xO_4$ nanoparticles and their magnetic, structural and dielectric properties. Physica B 588:412176
53. Asif M, Nadeem M, Imran M, Ahmad S, Musaddiq S, Abbas W, Khan MA (2019) Structural, magnetic and dielectric properties of NiCo doped BiFeO3 multiferroics synthesized via micro-emulsion route. Physica B Condens Matter 552:11–18
54. Junaid M, Nadeem M, Abubshait SA, Abubshait HA, Khan MA, Gilani ZA, Warsi MF (2020) Impact of Bi–Cr substitution on the structural, spectral, dielectric and magnetic properties of Y-type hexaferrites. Ceramics Int 46(16):25478–25484